Inhalable explosive nanosensor for real-time visual monitoring of therapeutic effects of lung cancer

Jukun Yang [a], Mo Ma [a,b], Chen Zhao [a], Jingkang Li [a], Yuxuan Chen [a], Zhuoxin Ye [a], Pinyi Ma [a,*], Daqian Song [a,*]

[a] College of Chemistry, Jilin Province Research Center for Engineering and Technology of Spectral Analytical Instruments, Jilin University, Qianjin Street 2699, Changchun 130012, China
[b] School of Pharmacy, Jilin University, Qianjin Street 2699, Changchun 130012, China

ARTICLE INFO

ABSTRACT

Lung cancer, as one of the major diseases that endanger human health, has a very high fatality rate. Consequently, effective evaluation of clinical treatment outcomes for lung cancer is crucial for the formulation of subsequent treatment plans for patients. In this work, we utilized amorphous calcium carbonate nanoparticles ($CaCO_3$ NPs) as sources of calcium ions (Ca^{2+}) to develop CPs ($CaCO_3$@PDA) core–shell nanoprobes. Concurrently, we functionalized the surface of gold nanoparticles with Cy5.5-peptide, AS1411, and (4-aminosulfonylphenyl) boronic acid (4-APBA) to produce APAAs (Au NPs@pep-AS1411-(4-APBA)), which were further assembled with CPs using PEG to construct an innovative explosive nanosensor, CPAs ($CaCO_3$@PDA-APAAs). The CPs component of the nanosensor could cause the release of a substantial amount of Ca^{2+} in response to the tumor microenvironment (TME), which in turn induced cellular Ca^{2+} overload and subsequent apoptosis. This event triggers caspase-3 activation, causing the cleavage of a specific peptide sequence (DEVD), resulting in the fluorescence signal being reinstated. Additionally, the 4-APBA moiety on the probe interacted with H_2O_2 resulting in alterations in surface-enhanced Raman spectroscopy (SERS) signals, which aided in the detection of reactive oxygen species (ROS) during the physiological processes. By utilizing atomization, the nanoprobes were strategically deposited in the affected lung regions to enhance the fluorescence imaging capabilities and effectively mirror the therapeutic outcomes. Overall, the CPAs explosive nanosensor has a potential in advancing the non-invasive visual monitoring of lung cancer prognosis and can be a valuable tool in ongoing efforts to improve the management of this challenging disease.

1. Introduction

Lung disease, particularly lung cancer, represents a major health challenge, as it is one of the most common cancers and the leading cause of cancer-related deaths worldwide [1,2]. Currently, surgery, radiotherapy, and chemotherapy are the cornerstone of lung cancer treatment [3]. However, the prognosis of the disease plays a crucial role in influencing survival rates of patients. Despite their significant advancements, the application of traditional diagnostic modalities such as computed tomography (CT) and magnetic resonance imaging (MRI) are still limited due to the risks of high radiation exposure and the complexity of quantitative analysis, the factors that render them as less suitable for frequent and direct prognosis evaluation [4–10]. Therefore, it is crucial to develop more intuitive and effective strategies for the precise

evaluation of clinical treatment outcomes in lung cancer [11,12]. These strategies are essential for informing and adjusting subsequent treatment plans, timely modifying patient treatment regimens, and ultimately improving patient survival rates [13–15].

Fluorescence imaging (FI) emerges as a promising candidate in this regard, owing to its cost-effectiveness, exceptional local imaging capabilities, and compatibility with nanosensor integration, and for these reasons, it is frequently utilized in disease diagnosis and monitoring [16–18]. Advancements in nanotechnology have ushered in an era of innovative nanoprobes with drug delivery capability through self-assembly or electrostatic adsorption to enable the modulation of vital cellular processes such as oxidative stress and apoptosis [19–22]. These processes, which are often marked by changes in biomarker levels, have underscored the critical role of precise biomarker detection. Moreover,

conjugating fluorescence molecules with nanosensors can enhance the utilization of FI and promote its advancement in the disease diagnosis and evaluation.

One of the challenges in biomedical diagnostics is the simultaneous monitoring of cellular apoptosis and oxidative stress, both of which are crucial for the understanding of disease progression [23,24]. To address this issue, we developed an innovative visual platform that can concurrently detect caspase-3 and hydrogen peroxide (H_2O_2), which are the markers of apoptosis and oxidative stress, respectively [25–28]. The assessment of cellular physiological states also necessitates the involvement of various ions prevalent in the physiological environment [29,30]. The metabolism of metal ions plays a vital role in numerous physiological processes, as the homeostasis of calcium ions (Ca^{2+}) can affect the cellular oxidative balance. Abnormal accumulation leads to Ca^{2+} overload that can disrupt this homeostasis and result in increased levels of reactive oxygen species (ROS), which can ultimately lead to cell apoptosis [31,32]. In this study, we leveraged this physiological process by using pH-responsive amorphous calcium carbonate nanoparticles ($CaCO_3$ NPs) as one of the components of our probes. These $CaCO_3$ NPs can respond to the weakly acidic environment of the tumor microenvironment (TME) by releasing Ca^{2+} and CO_2 and thus can act as an exogenous source of Ca^{2+} and indicators for detecting changes in caspase-3 and H_2O_2 levels during autogenous physiological processes.

To enhance its biocompatibility, $CaCO_3$ NPs were modified with a polydopamine (PDA) shell. When $CaCO_3$ NPs@PDA (CPs) were in an acidic environment, an explosive-like reaction occurs, resulting in the release of a large amount of Ca^{2+}. The surface of gold nanospheres was modified with AS1411 (a tumor-targeting moiety), Cy5.5-pep, and surface-enhanced Raman spectroscopy (SERS) signaling molecules 4-APBA (a H_2O_2-responsive moiety) to form APAAs (Au NPs@pep-AS1411-(4-APBA)). These nanoparticles were assembled with polyethylene glycol (PEG) to create an explosive nanosensor, namely CPAs. CPAs could be administered noninvasively through atomization, which could allow for efficient enrichment of the nanoprobes in the lungs. The fluorescence of Cy5.5 was quenched due to the Förster resonance energy transfer (FRET) effect and was only recovered after caspase-3 activation and peptide chain cleavage. This process enables the effective visual evaluation of the treatment and prognosis. Additionally, the introduction of CPs allows for a significant link between TME-induced Ca^{2+} overload and imaging. The TME-responsive explosive nanosensor CPAs with imaging capabilities can be employed to facilitate the evaluation of the prognostic efficacy of pulmonary diseases.

2. Materials and methods

2.1. Synthesis of CPs

Initially, 1 mL of 2 mg/mL synthesized $CaCO_3$ NPs (see Supporting Information) was prepared [33]. The NPs were then uniformly dispersed in 50 mL of Tris-HCl buffer solution (10 mM, pH 8.5). While stirring, 10 mL of dopamine hydrochloride (0.5 mg/mL) was incrementally added to the dispersion. The mixture was then stirred vigorously for 4 h to allow for the polymerization of dopamine on the surface of $CaCO_3$ nanoparticles to form a polydopamine (PDA) coating. Following the completion of the reaction, CPs were isolated by centrifugation at 8000 rpm for 10 min and subsequently washed to remove any unreacted substances. The final product was re-dispersed in ultrapure water for further characterization or application.

2.2. Synthesis of CPAs (CPs-APAAs)

To begin with, 5 mL of 2 mg/mL CPs was thoroughly mixed with 20 mL of 2 mg/mL APAA solution (see Supporting Information). Subsequently, 60 μL of HS-PEG-NH₂ (1.0 mM) was added to the mixture to facilitate the conjugation process. The mixture was then continuously stirred for 12 h at ambient temperature to ensure the efficient binding of HS-PEG-NH₂ to the nanoparticles. After the reaction was complete, CPAs were isolated by centrifugation at 8000 rpm for 10 min. The pellet obtained was washed to remove any unbound reactants and finally re-dispersed in ultrapure water for subsequent use or analysis.

2.3. In vitro sensing of caspase-3 by CPAs

The CPAs probe was dispersed in a reaction buffer (300 μL, pH 7.2) comprising 50 mM HEPES, 10 mM EDTA, 50 mM NaCl, 5 % glycerol, and 0.1 % CHAPS to a concentration of 100 μg/mL. The solution was then incubated with 200 ng/mL caspase-3 at 37°C. To determine the optimal reaction time, the fluorescence intensity was recorded after 5, 10, 20, 30, 60, and 90 min, with 60 min being the ideal duration that led to peak fluorescence intensity. The response of CPAs to caspase-3 at various concentrations (0 to 500 ng/mL) was also investigated under the same conditions, and the fluorescence was measured after 60 min of incubation. Specificity and interference resistance tests were conducted by incubating CPAs with a variety of biomolecules and substances, including MUC1 protein, various miRNAs (miRNA21, miRNA105, miRNA210), CES1, ALP, BChE, BSA, glucose, and caspase-3 combined with its specific inhibitor Z-DEVD-FMK at 37°C. The concentration of miRNAs was 20 μM, whereas that of other potential interferents was 200 ng/mL. The effect of 50 μM Z-DEVD-FMK on the CPAs-caspase-3 system was also assessed. Lastly, the storage stability of CPAs was evaluated under different storage conditions, by which the fluorescence response was examined after storage for 1, 3, 5, and 7 days at temperatures of 25°C, 37°C, 45°C, and 55°C, to assess the probes' reliability over time.

2.4. In vitro sensing of H_2O_2 by CPAs

Initially, the CPAs probe at a concentration of 100 μg/mL (diluted in 600 μL of water), was reacted with 1 mmol/L H_2O_2 at 25°C. The SERS signal of the reaction was then recorded after 5, 10, 30, 60, 90, and 120 min, and the optimal reaction time was determined (which was found to be 60 min). Subsequently, CPAs were exposed to H_2O_2 at various concentrations (0 to 1000 μM) under the same conditions for 60 min. The SERS signal intensity of the mixture was then measured in order to evaluate the probes' sensitivity to H_2O_2. To assess its specificity and interference resistance, the CPAs probe was incubated with potential interferents including MUC1 protein, miRNAs (miRNA21, miRNA105), BSA, and ions (Ca^{2+}, CN^-, Cu^{2+}), as well as ALP, BChE, glucose, and caspase-3. The concentrations of the interferents used for the tests were as follows: 20 μM for miRNAs, 10 mM for ions, and 200 ng/mL for other substances. The SERS signals were subsequently analyzed in order to confirm the probes' specificity and anti-interference capabilities and ensure its accuracy in H_2O_2 detection in complex biological matrices.

2.5. Cell imaging applications

Initially, the optimal incubation time for A549 cell imaging was determined through a time-course experiment. Cells were incubated with 100 μg/mL probe for various durations: 6, 12, 24, and 36 h. Based on the fluorescence signal intensity, a 24-h incubation period was selected. Subsequently, A549 cells were treated for 24 h with APAAs, APAAs plus *cis*-platinum (CDDP), CPAs, and CPAs plus Z-DEVD-FMK at the following concentrations: 100 μg/mL for APAAs and CPAs, 20 μM for CDDP, and 50 μM for Z-DEVD-FMK. Cells in the APAAs + CDDP group acted as the positive control, while untreated cells served as the negative control. Fluorescence imaging was then performed at an excitation wavelength of 670 nm.

2.6. In vivo imaging applications

Among them, the control group was set as mice without tumor after inhalation of CPAs for imaging. Meanwhile, tumor-bearing mice were

exposed to atomized CPAs (200 μg/mL, 8 mL) via an atomizing device. After inhalation, the mice were anesthetized with isoflurane and then subjected to fluorescence imaging after 1, 2, and 3 h; and the imaging efficacy was evaluated thereafter. APAAs alone and in combination with CDDP (APAAs: 200 μg/mL, 8 mL; CDDP: 20 μM) were also atomized and administered to another set of tumor-bearing mice; and this was followed by fluorescence imaging. To assess the pulmonary localization efficiency via inhalation, Cy5.5-labeled CPs (200 μg/mL, 50 μL) were administered intravenously through the tail vein. Fluorescence imaging was carried out post-anesthesia to allow for a comparative analysis between inhalation and intravenous injection based on organ imaging results.

3. Results and discussion

3.1. Synthesis and characterization of CPAs

The synthesis of CPAs is depicted in Scheme 1, with the initial step involving the production of $CaCO_3$ NPs via the gas diffusion method. The SEM image revealed that $CaCO_3$ NPs exhibited a uniform and monodisperse distribution, had milky white appearance in ethanol (Fig. S1), and had an average size of 95.2 ± 0.8 nm (Fig. S2A). Subsequent modification with PDA under alkaline conditions not only enhanced the water dispersion capabilities of NPs but also caused their color to change to brown, as evidenced in Fig. S1. This surface modification was further confirmed by the change in zeta potential to -12.6 mV (Fig. 1H), which was indicative of the presence of PDA shell. At the same time, in order to

explain the collapse of $CaCO_3$ structure in CPs under acidic conditions, we treated CPs (PBS, pH 6.8, 1 h) and characterized with SEM. The results showed (Fig. S3) that NPs treated under acidic conditions showed obvious structural damage, which also confirmed the response of CPs to acidic environment. At the same time, in order to further proved the structural stability of the probe, we treated the probe with cell culture medium and conducted TEM imaging. The results were shown in Fig. S4, and the detection results of UV–vis absorption spectrum also proved that the complex environment did not affect the structural stability of the probe.

The synthesis of 20 nm Au NPs was achieved by reducing chloroauric acid with sodium citrate, which yielded wine-red nanoparticles with a zeta potential of -12.3 mV. These NPs, as shown in the TEM image (Fig. 1B), had an average size of 20.4 ± 0.2 nm (Fig. S2). The enhancement of stability of Au NPs was achieved through the modification with mPEG-SH, followed by the conjugation with Cy5.5-pep and AS1411 to form APAs. The functionalization process was successful, as evidenced by the shift in the zeta potential to -25.4 mV (Fig. 1H), which was the signal for the successful attachment of the negatively charged molecules. Further modification with 4-APBA to obtain APAAs. The experimental results showed that APAAs was same as APAs, there was no significant change in the position of UV–vis peak. The zeta potential of APAAs changed slightly to -23.7 mV (Fig. 1F, H).

The final assembly of CPAs, which involved the mixing of CPs, APAAs, and HS-PEG-NH$_2$, was confirmed by TEM analysis (Fig. 1C). The analysis revealed the distribution of APAAs on the CP surface, causing CPAs to have an average size of approximately 200 nm and a zeta
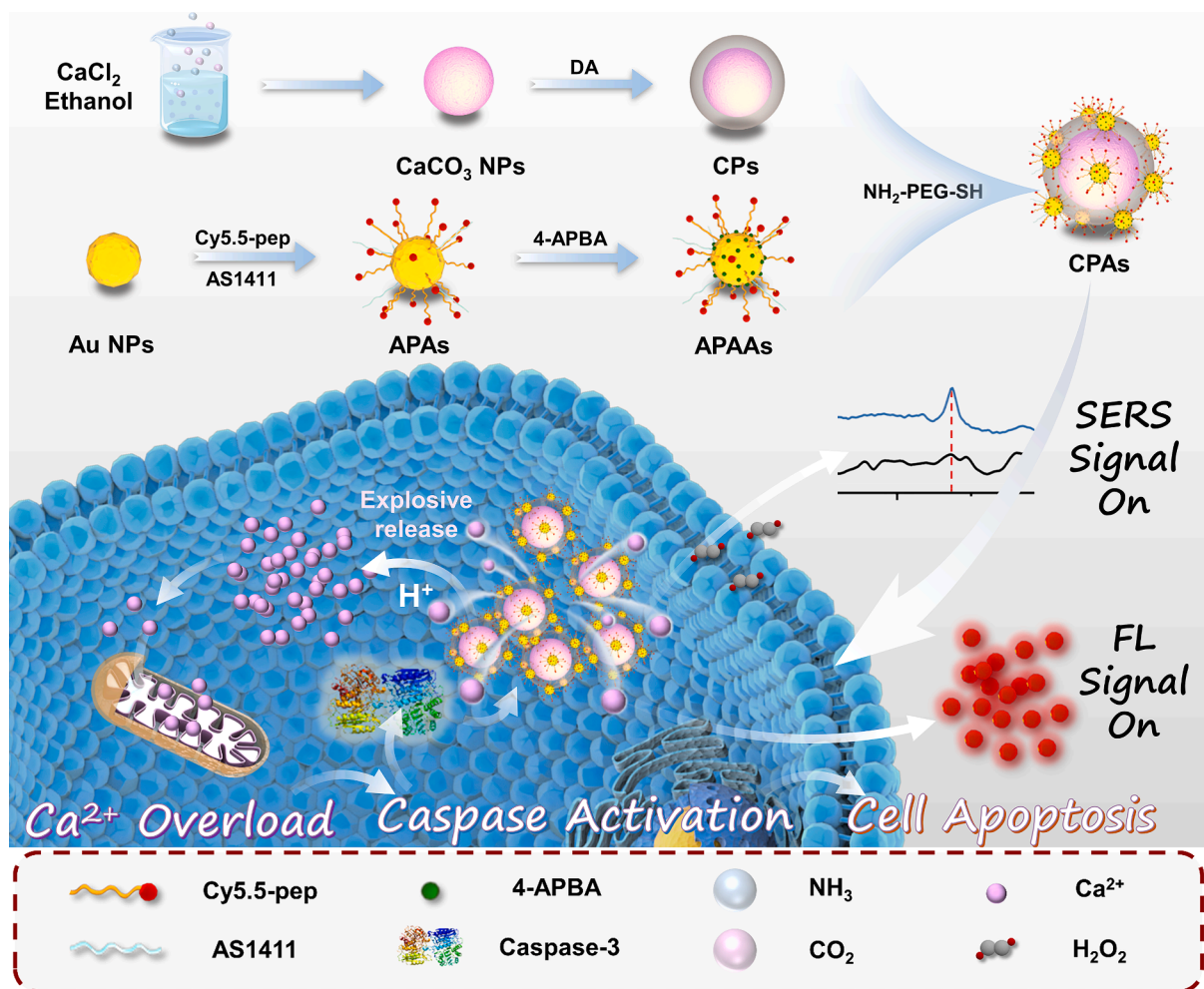
Scheme 1. Schematic illustration of the synthesis process and application of CPAs.
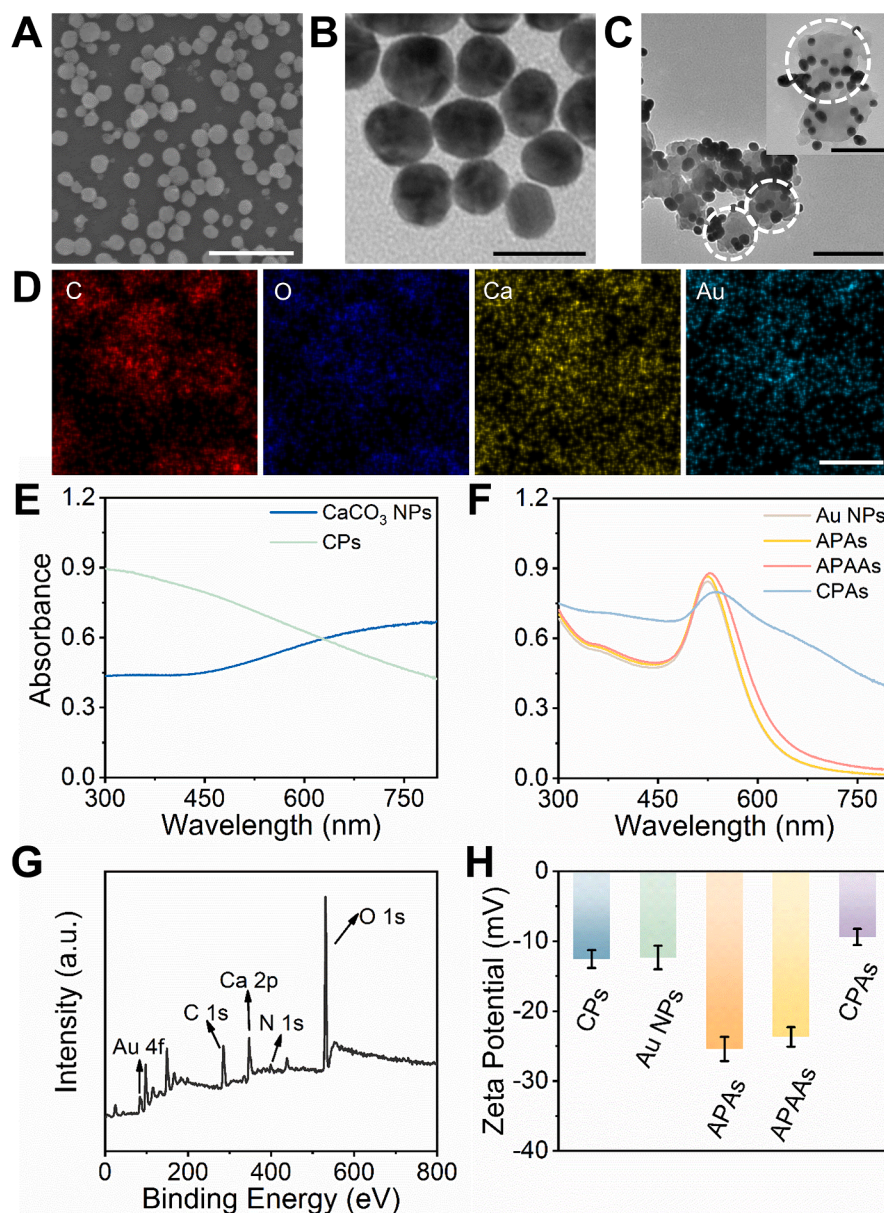
Fig. 1. Scanning electron microscopic (SEM) image of (A) CaCO₃ NPs (scale bar: 500 nm). Transmission electron microscopic (TEM) images of (B) Au NPs (scale bar: 50 nm) and (C) CPAs (scale bars: 300 nm and 200 nm). (D) Elemental mapping of CPAs. UV–vis absorption spectra of (E) CaCO₃ NPs and CPs, (F) Au NPs, APAs, APAAs, and CPAs. (G) XPS spectrum of CPAs. (H) Zeta potential of CPs, Au NPs, APAs, APAAs, and CPAs.

potential of −9.4 mV. Elemental analysis (Fig. 1D and S5) confirmed the presence of key elements (C, O, Ca, Au), which validated the successful synthesis of CPAs. This was further supported by XPS data (Fig. 1G and S6), which detailed the elemental composition and corroborated the effectiveness of the synthesis method. Notably, the APAAs modification resulted in a discernible change in the UV–vis peak of the nanoparticles (Fig. 1F), along with a transformation in color to black-purple (Fig. S1), which collectively confirmed the successful synthesis of CPAs.

3.2. In vitro sensing ability of nanosensors

Detection of caspase-3: To augment the imaging capability of the Ca²⁺ overload detection nanoprobes, Cy5.5-pep, which could be recognized by caspase-3, was conjugated to the nanoparticles. This design leveraged the FRET phenomenon, where Cy5.5 fluorescence was quenched by adjacent Au NPs. Upon caspase-3 activation, which caused the cleavage of the peptide linker, the fluorophore was released, leading to the restoration of fluorescence. This mechanism was emulated by

introducing caspase-3 to simulate its activation during Ca²⁺ overload-induced apoptosis to facilitate the *in vitro* fluorescence sensing of CPAs in a solution.

An initial investigation into the influence of reaction time on the fluorescence ratio (F_R) revealed a time-dependent increase in F_R values ($F_R = (F − F_0)/F_0$), where F represented the post-reaction fluorescence intensity and F_0 was the control fluorescence intensity without enzyme. A plateau in fluorescence signal intensity was observed at 60 min, an indication that the optimal reaction time for maximal signal recovery is 60 min (Fig. 2A). Subsequent experiments, in which caspase-3 concentration was varied, demonstrated a concentration-dependent increase in F_R when the caspase-3 concentration was within a 0–500 ng/mL range. A linear relationship was observed at caspase-3 concentrations between 0 and 100 ng/mL, and the limit of detection (LOD) was 0.208 ng/mL (S/N = 3), which is comparable to that of the probes reported in the literature (Fig. 2B-C) [34,35].

The selectivity of the nanoprobes to caspase-3 was further validated by substituting caspase-3 with various biomarkers and observing
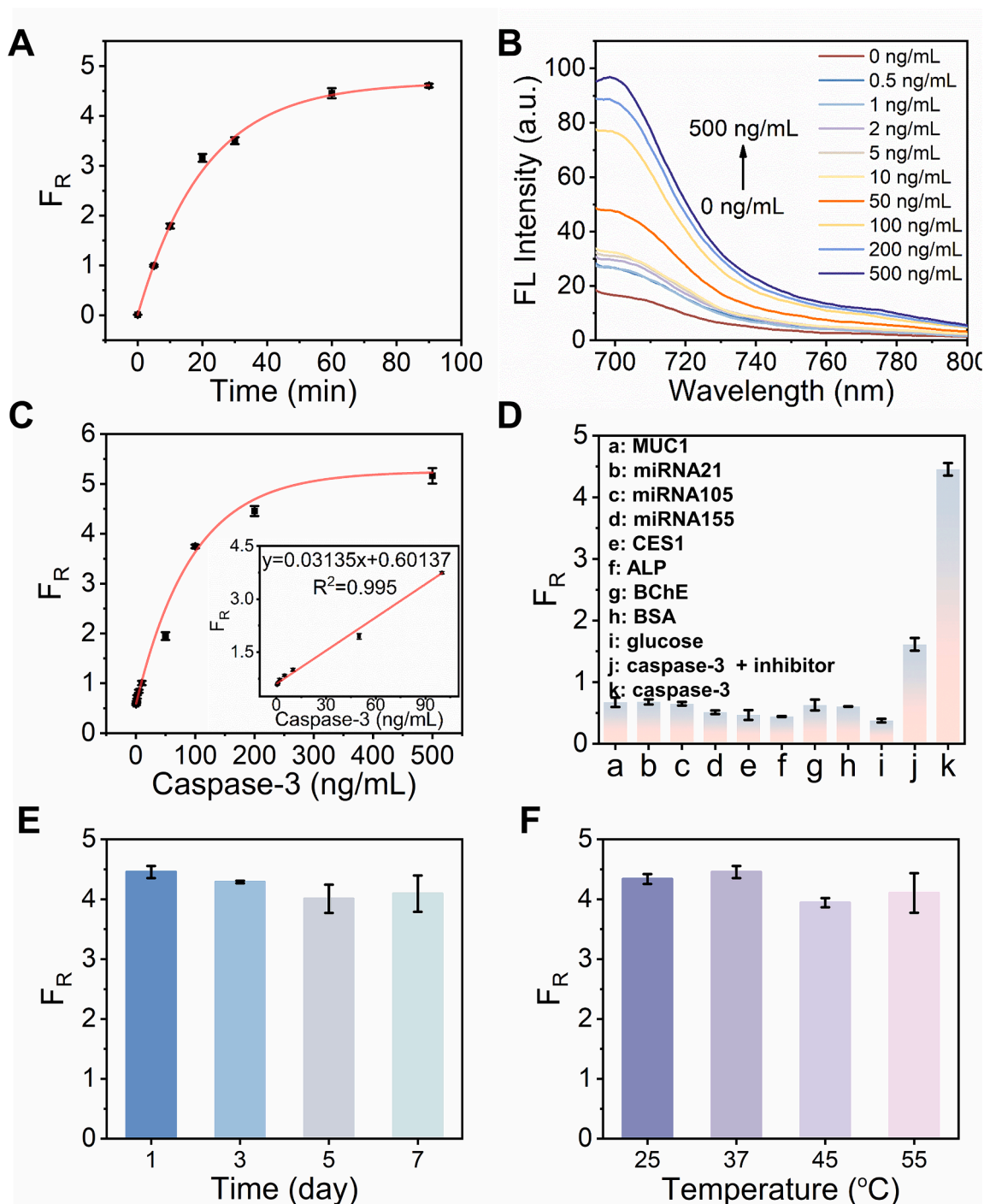
Fig. 2. (A) Time-dependent F_R response of CPAs in the presence of caspase-3 at 37°C. (B) Fluorescence spectra of CPAs in the presence of caspase-3 with increasing concentrations from 0 to 500 ng/mL and (C) the corresponding F_R response. The inset displays the linear relationship between F_R and caspase-3 concentration. (D) Selectivity of CPAs towards various enzymes and substances (a: Mucin-1 (MUC1); b: miRNA21; c: miRNA105; d: miRNA155; e: carboxylesterase 1 (CES1); f: alkaline phosphatase (ALP); g: butyryl cholinesterase (BChE); h: bovine serum albumin (BSA); i: glucose; j: caspase-3 + inhibitor (Z-DEVD-FMK); k: caspase-3). The error bars represent standard deviation (n = 3). F_R plot of nanoprobes upon treatment with caspase-3 under different conditions. (E) Time. (F) Temperature.

negligible fluorescence response, the indication of minimal interference. Notably, co-incubation with Z-DEVD-FMK (a caspase-3 inhibitor) markedly diminished the fluorescence signal, and this underscored the specificity of the probe to caspase-3 (Fig. 2D). Moreover, the robustness of CPAs was evaluated through repeated co-incubation experiments with caspase-3 under varying temporal and thermal conditions (Fig. 2E-F). These tests confirmed the high stability of the nanoprobe, which is essential for its applications.

Detection of H_2O_2: To achieve concurrent detection of H_2O_2, the

compound pivotal to the Ca^{2+} overload scenarios, CPAs were functionalized with a SERS-active molecule, 4-APBA. The functionalization enabled the direct observation of the interaction between H_2O_2 and 4-APBA, which manifested as a distinct Raman peak at 870 cm^{-1}, and allowed for the high sensitivity of the probe to H_2O_2 (Fig. 3A). Temporal analysis of the SERS signal intensity revealed a progressive increase of the signal until stabilizing at 60 min. This time point was thus selected in subsequent *in vitro* reactions, where H_2O_2 at varying concentrations was introduced to the nanoprobes. A concentration-dependent amplification
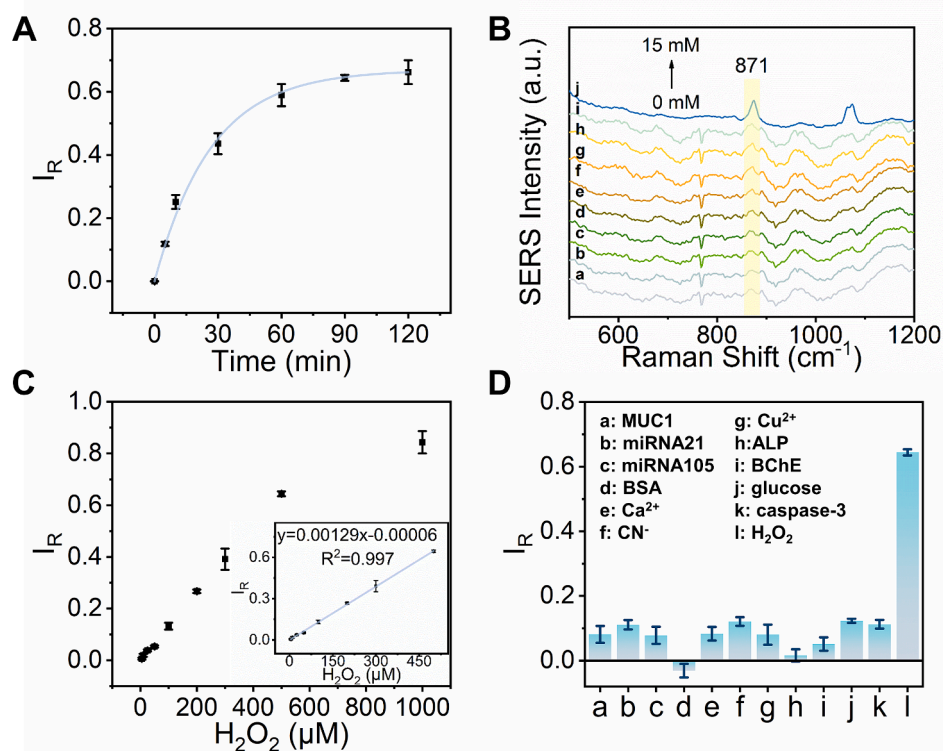
Fig. 3. (A) Time-dependent I_R response of CPAs in the presence of H_2O_2 at 25°C. (B) SERS signal of CPAs in the presence of H_2O_2 with increasing concentrations from 0 to 1000 μmol/L and (C) the corresponding I_R response. The inset displays the linear relationship between I_R and H_2O_2 concentration. (D) Selectivity of CPAs towards various enzymes and substances (a: MUC1; b: miRNA21; c: miRNA105; d: BSA; e: Ca^{2+}; f: CN^-; g: Cu^{2+}; h: ALP; i: BChE; j: glucose; k: caspase-3; and l: H_2O_2).

of the SERS signal was observed when H_2O_2 concentrations were within a 0–1000 μmol/L range. This illustrates the probes' capacity to accurately detect H_2O_2 levels (Fig. 3B-C). Further selectivity assays underscored the specificity of CPAs to H_2O_2, which allows it to distinguish H_2O_2 from other potential biological interferents (Fig. 3D). This specificity is crucial for reliable detection of H_2O_2 within the complex biochemical milieu of physiological processes. At the same time, the results of Fig. S8 also prove that as a probe for ROS detection, its performance was relatively stable, which was conducive to subsequent applications.

Collectively, the findings underscore the dual-functionality of CPAs: the detection of both caspase-3 and H_2O_2. This dual detection capability not only can enhance the utilization of CPAs in biomarker monitoring but also can signify their potential applicability in real-time monitoring of physiological processes. The ability to simultaneously track these biomarkers of CPAs can open new avenues for the understanding of the intricate dynamics of Ca^{2+} overload and its associated cellular responses, making them a valuable tool for biomedical research and diagnostics.

3.3. Sensing of H_2O_2 in cell lysates

Real-time monitoring of H_2O_2 is imperative due to its role as a vital physiological indicator. In this vein, we employed CPAs to evaluate H_2O_2 levels in cell lysates, aiming to validate the applicability of nanoprobes in live-cell applications. The H_2O_2 detection principle of CPAs is depicted in Fig. 4A, which highlights the probe's responsiveness to H_2O_2. Initial experiments focused on H_2O_2 produced in tumor cells, as triggered by phorbol-12-myristate-13-acetate (PMA). PMA is known to activate cellular redox signaling pathways, which lead to oxidative stress. As illustrated in Fig. 4B, CPAs could detect a marked increase in H_2O_2 levels upon PMA stimulation. The result confirms the probes' sensitivity to endogenous H_2O_2. Building upon this, we explored H_2O_2

modulation in response to various treatments, including different nanoparticles and *cis*-platinum (CDDP, a chemotherapeutic agent). The data (Fig. 4B), indicated elevated H_2O_2 levels, which underscores the impact of therapeutic agents on cellular oxidative states. Furthermore, the applicability of CPAs was extended beyond A549 cells, as demonstrated by successful H_2O_2 detection in lysates from two additional tumor cell lines. In addition, in order to further proved the applicability and ability of the probe to detect ROS, we designed a cell lysate labeling experiment to allow the probe to detect H_2O_2 in a complex environment. The specific experimental results were shown in Table S1. This versatility emphasizes the broad application range of the probe across diverse cell types.

3.4. Evaluation of cytotoxicity

Before cell imaging experiments, we explored the cytotoxicity of nanoprobes on A549 cells. The cell activity was detected by CCK-8 assay. The cells were treated with different concentrations of probes at different time (12, 24 h): APAAs, CPAs (12.5, 25, 50, 100, and 200 μg/mL); all of which showed no significant effect on cell survival. As shown in Fig. S9A, when the nanoprobe concentration reached 100 μg/mL (24 h), the cell survival rate was also higher than 83%. This result suggested that the nanoprobes, at concentrations suitable for imaging applications, had no significant impact on cell viability. Fig. S9B showed that the introduction of CPs in CPAs leads to a significant decrease in cell viability, which corresponded to the result that Ca^{2+} overload induced cell death. The effect of CPAs on cell viability was demonstrated. This favorable cytotoxicity profile paves the way for further investigation on their intracellular utilization in detail, with an aim to enable the real-time monitoring of cellular processes with minimal perturbation to the cellular environment.
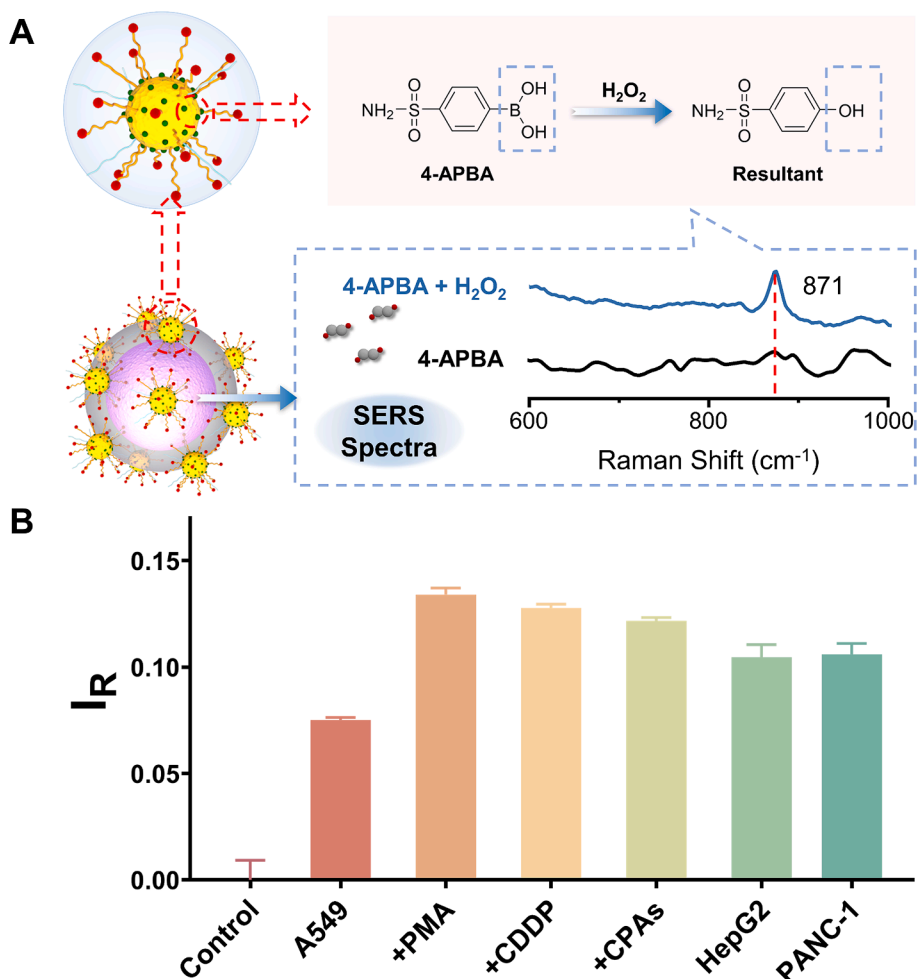
Fig. 4. (A) Schematic diagram illustrating the SERS signal response of CPAs. (B) I_R of cell lysate under different conditions.

3.5. Cell imaging applications

Lung cancer poses a serious threat to human life and health, thereby necessitating the development of advanced diagnostic tools for real-time monitoring of cancer cell physiology. In this context, CPAs, equipped with CaCO$_3$ NPs, could be a promising tool for probing the tumor microenvironment. As depicted in Fig. 6A, the nanoprobes responded to the unique conditions within the tumor by potentially triggering intracellular Ca^{2+} overload. This induced the activation of the caspase

pathways, which in turn led to cell apoptosis. Crucially, CPAs enabled the real-time imaging of caspase-3 activity, a key player in the apoptotic process, and provided valuable insights into the cellular response to cancer therapies.

To validate the hypothesis that CPAs could detect caspase-3 activation via Ca^{2+} release, A549 lung cancer cells were incubated with the nanoprobes. First, the incubation time was optimized, and the results were shown in Fig. 5A-B. And 24 h was selected as the incubation time. The observed fluorescence signals (Fig. 6B), confirmed the activation of
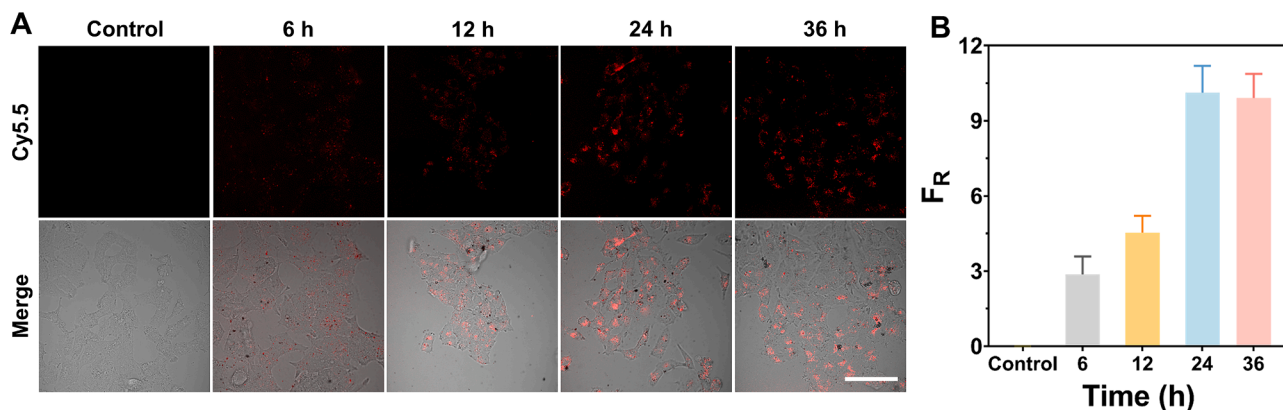
Fig. 5. (A) Fluorescence microscope images incubated with CPAs for different time. Scale: 100 μm (B) Corresponding F_R of A549 cells under different incubation time.
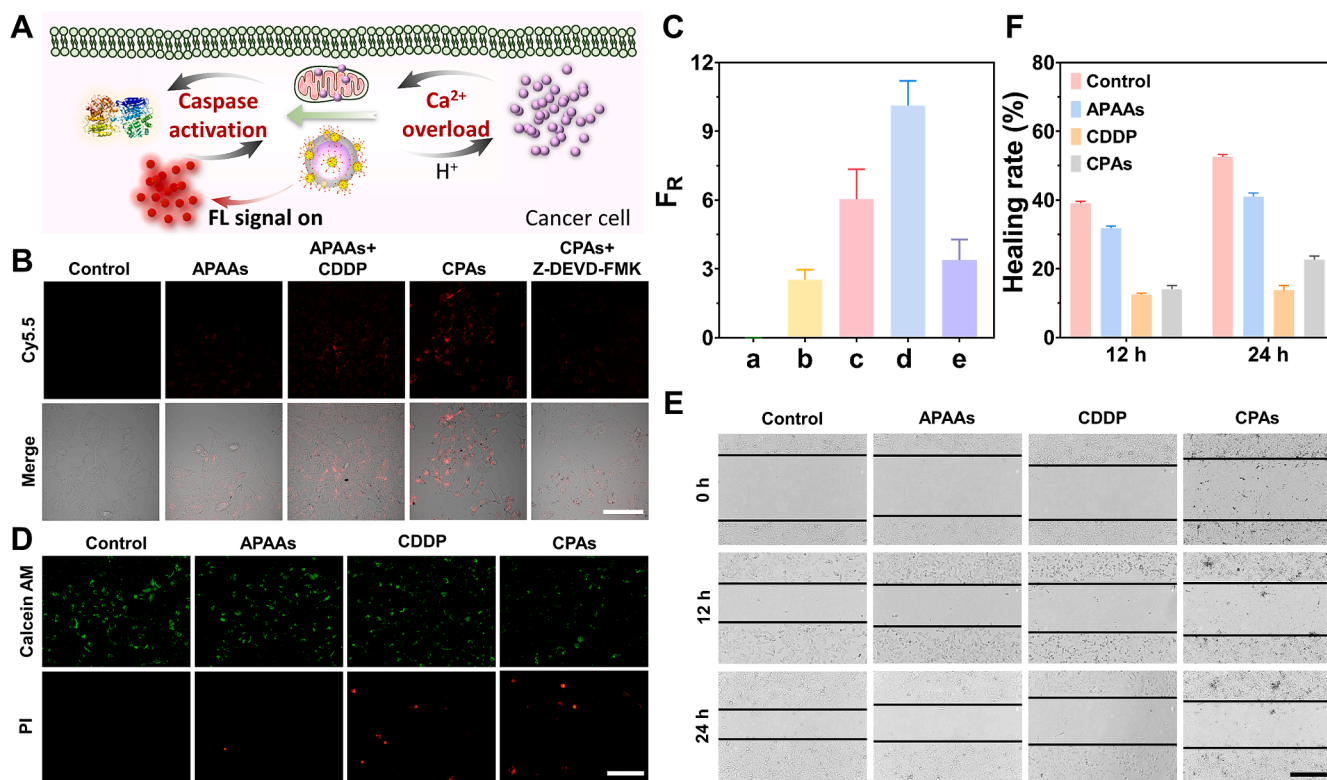
Fig. 6. (A) Schematic diagram depicting the fluorescence recovery of probes induced by Ca^{2+} overload-triggered caspase activation in A549 cells. (B) Fluorescence microscopic images of A549 cells under various treatments. Scale bar: 100 μm. (C) The corresponding F_R of A549 cells in (B) under different conditions (a: control; b: APAAs; c: APPAs + cisplatin; d: CPAs; and e: CPAs + Z-DEVD-FMK). (D) Live/dead staining of A549 cells under various treatment conditions for 24 h: Calcein-AM (green, live cells), PI (red, dead cells). Scale bar: 150 μm. (E) Photographs of wound healing under different conditions for various durations (0, 12, and 24 h). Scale bar: 300 μm. (F) Healing rate of wound in each group.

caspase-3 in response to Ca^{2+} surges. To enhance the reliability of these findings, additional experiments were conducted using APAAs and APAAs combined with cisplatin (CDDP), which was a chemotherapeutic agent known to induce apoptosis. CDDP-treated cells, which was served as the positive control for chemotherapy efficacy, caused significant fluorescence enhancement. This observation underscored the sensitivity of the nanoprobes to the apoptosis markers (Fig. 6B-C). The introduction of Z-DEVD-FMK, a caspase-3 inhibitor, further confirmed our findings, as it significantly diminished the fluorescence signal. This affirms the specificity of CPAs towards caspase-3 activity.

In addition to fluorescence imaging, cell viability assays using calcein AM/propidium iodide (PI) staining and scratch migration tests were performed on different treated cells. The results (Fig. 6D-F) revealed minimal impact of the probes on cell viability in the absence of $CaCO_3$ NPs. However, the introduction of $CaCO_3$ NPs led to a marked reduction in cell activity and viability, which aligns with the hypothesized mechanism of Ca^{2+} overload-induced apoptosis. These comprehensive analyses highlight the potential of CPAs as not only a diagnostic tool for lung cancer but also a method for evaluating therapeutic efficacy. They also lay the groundwork for the adoption of CPAs in clinical and research environments dedicated to cancer treatment and monitoring.

3.6. Hemolysis assay

In the transition to *in vivo* imaging applications following successful cell imaging, assessing the biocompatibility of the nanoprobes is crucial. Thus, a hemolysis assay was conducted as a preliminary evaluation. The results, depicted in Fig. S10, demonstrated minimal hemolytic activity, affirming the biocompatibility of the probes. This finding supports the feasibility in advancing into *in vivo* imaging studies with these nanoprobes.

3.7. In vivo imaging applications

Building on the promising outcomes of cell imaging studies, we carried out *in vivo* experiments to explore the ability of the nanoprobes in visualizing lung cancer in a mouse model. Traditional approaches often rely on tail vein injections for probe delivery, which can lead to suboptimal accumulation of probes in the target tumor site. To address this issue and enhance the probe delivery to the lungs, we employed an atomization technique, which is a technique that allows for direct inhalation of the nanoprobes by mice, for more effective localization and enrichment within the lung tissues.

We established an in-situ lung cancer mouse model for this purpose, as depicted in Fig. 7A. The experimental setup is illustrated in Fig. 7B. Different formulations, including APAAs combined with cisplatin (CDDP) and CPAs, were administered to mice via atomization before imaging. Non-tumor mice that inhaled CPAs served as the negative control, exhibited negligible fluorescence, as shown in Fig. 7C. The addition of CDDP with an intention to validate the chemotherapeutic efficacy led to significant fluorescence recovery in both the CDDP and CPAs-treated groups. This observation indicates the probes' effectiveness in monitoring the treatment response.

To underscore the benefits of atomization inhalation for probe enrichment in the lungs, we compared its effects with those of traditional tail vein injection. Cy5.5-tagged CPs were administered via tail vein, and the administration resulted in predominant fluorescence in the abdominal region. Comparing organ images resulted from the tail vein and inhalation methods revealed distinct localization patterns: the tail vein group exhibited fluorescence mainly in the liver, whereas inhalation led to a pronounced signal in the lungs (Fig. 7D). This stark difference underscores the superiority of the inhalation method in targeting lung tissue.
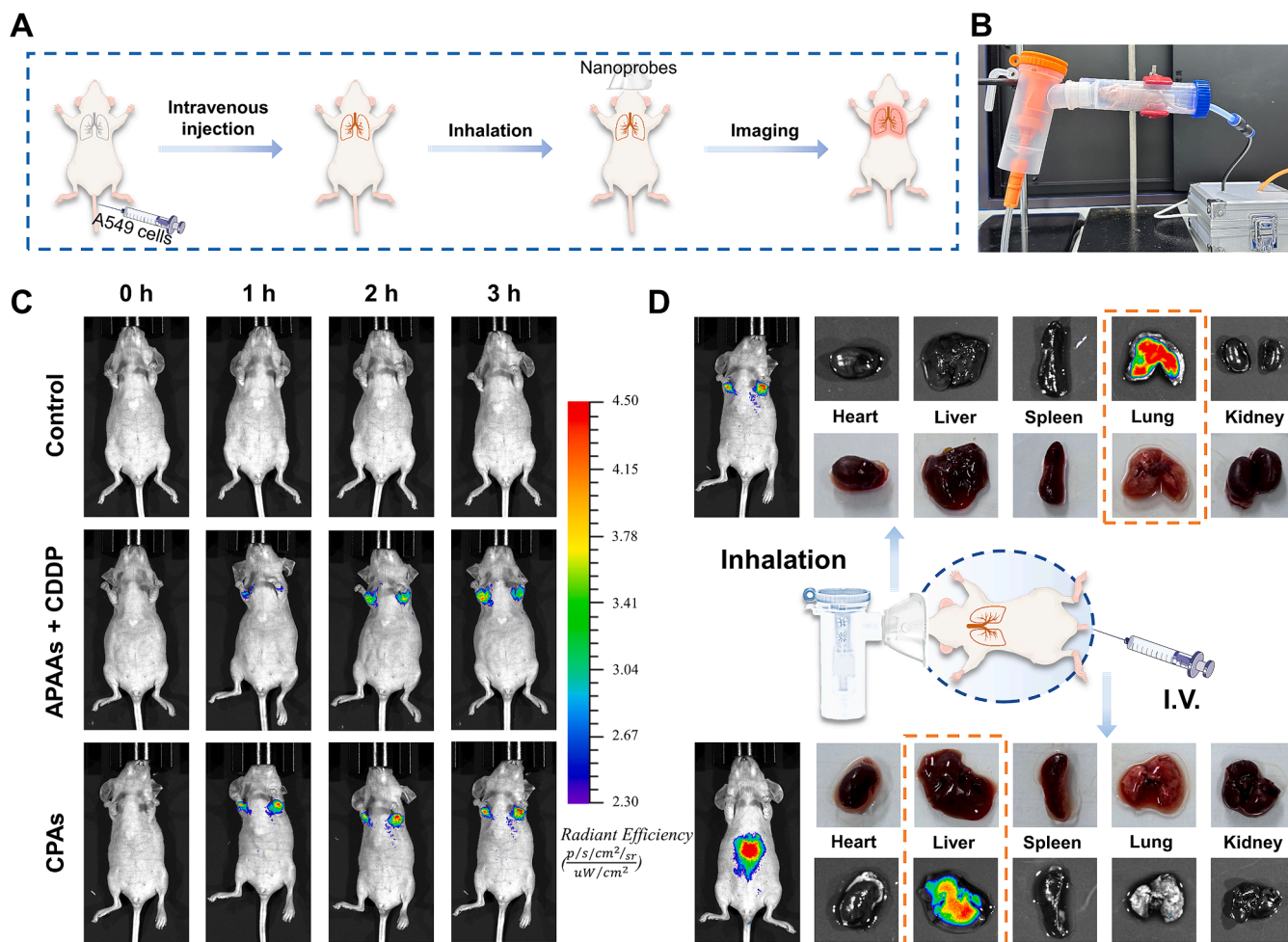
Fig. 7. (A) Evaluation of therapeutic effects on *in situ* lung cancer model through imaging (the nanoprobes were atomized and inhaled by mice). (B) Digital images of the inhalation device. (C) Fluorescent images of mice inhaled with nanoprobes for different times. (D) *In vitro* fluorescence images of mouse organs isolated after inhalation and injection.

In summary, the *in vivo* imaging results aligned with the cell imaging findings, which reinforced the potential of CPAs in real-time visual monitoring in lung cancer research and treatment. This novel inhalation approach not only improves the delivery of probe to lung tissues but also presents a new avenue for non-invasive imaging strategies in oncology.

4. Conclusion

In this study, we developed and characterized a novel inhalable explosive nanosensor, CPAs, tailored for the visual evaluation of therapeutic effects of lung cancer. The nanosensor consisted of core–shell nanoparticles and $CaCO_3$ NPs enveloped in a PDA layer, which functioned as a source of Ca^{2+} ions. This design was pivotal to the triggering of intracellular Ca^{2+} surges, which was necessary for the activation of apoptotic pathways and subsequent caspase-3 activation. The enzymatic activity leaded to the cleavage of a specifically designed peptide linker, liberating the fluorophore that in turn reinstated the fluorescence signal, which was a direct indicator of caspase-3 activity. Furthermore, the incorporation of 4-APBA allowed the nanosensor to interact with H_2O_2, which caused distinct changes in the SERS signal. This feature added a layer of functionality to the nanosensor by allowing it to concurrently monitor H_2O_2 level, a critical indicator of oxidative stress associated with cancer progression. The efficacy of the nanosensor was validated both *in vitro* (buffer and cells) and *in vivo* (mouse models). By utilizing atomization, this method could ensure non-invasive and targeted deposition within lung tissues. This nanosensor not only allows for successful lung imaging but also is a representation of a promising non-invasive strategy for monitoring the therapeutic effects of lung cancer treatments.

CRediT authorship contribution statement

Jukun Yang: Writing – original draft, Investigation, Formal analysis, Data curation, Conceptualization. **Mo Ma:** Investigation, Data curation. **Chen Zhao:** Investigation, Data curation. **Jingkang Li:** Investigation, Formal analysis. **Yuxuan Chen:** Investigation. **Zhuoxin Ye:** Investigation. **Pinyi Ma:** Writing – review & editing, Project administration, Data curation, Conceptualization. **Daqian Song:** Supervision, Resources, Project administration, Funding acquisition.

Declaration of competing interest

The authors declare that they have no known competing financial interests or personal relationships that could have appeared to influence the work reported in this paper.

Data availability

Data will be made available on request.

Appendix A. Supplementary data

Supplementary data (Materials, instruments, synthesis of CaCO$_3$ NPs, synthesis of Au NPs, synthesis of APAAs, detection of H$_2$O$_2$ in cell lysates, CCK-8 assay, *in vitro* migration assay, calcein AM/propidium iodide (PI) staining, hemolysis assay, establishment of tumor model, supplementary figures and references) to this article can be found online at https://doi.org/10.1016/j.cej.2024.153747.

References

[1] A.A. Thai, B.J. Solomon, L.V. Sequist, J.F. Gainor, R.S. Heist, Lung cancer, Lancet 398 (10299) (2021) 535–554.

[2] R.D. Neal, F. Sun, J.D. Emery, M.E. Callister, Lung cancer, BMJ-Br. Med. J. 365 (2019) I1725.

[3] A. Singareddy, M.E. Flanagan, P.P. Samson, S.N. Waqar, S. Devarakonda, J. P. Ward, B. Herzog, A. Rohatgi, C.G. Robinson, R. Govindan, V. Puri, D. Morgensztern, Trends in stage I lung cancer, J. Clin. Oncol. 40 (16) (2022).

[4] D. Pan, E. Roessl, J.P. Schlomka, S.D. Caruthers, A. Senpan, M.J. Scott, J.S. Allen, H.Y. Zhang, G. Hu, P.J. Gaffney, E.T. Choi, V. Rasche, S.A. Wickline, R. Proksa, G. M. Lanza, Computed tomography in color: Nanok-enhanced spectral CT molecular imaging, Angew. Chem. Int. Edit. 49 (50) (2010) 9635–9639.

[5] S.P. Kwon, S. Jeon, S.H. Lee, H.Y. Yoon, J.H. Ryu, D. Choi, J.Y. Kim, J. Kim, J. H. Park, D.E. Kim, I.C. Kwon, K. Kim, C.H. Ahn, Thrombin-activatable fluorescent peptide incorporated gold nanoparticles for dual optical/computed tomography thrombus imaging, Biomaterials 150 (2018) 125–136.

[6] C. Wang, J. Zhu, S. Wang, L. Zhao, P. Wei, T. Yi, Self-assembled nano-CT contrast agent leveraging size aggregation for improved in vivo tumor CT imaging, Adv. Mater. 36 (2023) 2309789.

[7] Y.B. Liu, X. Jiang, W. Wang, W. Zhang, P.Y. Ma, Y.B. Huang, D.Q. Song, Single-trigger dual-modal nanoplatform for in situ switch on cancer diagnosis imaging, Sens. Actuat. B-Chem. 381 (2023) 133420.

[8] D.X. Chen, Y.Y. Lin, A. Li, X.J. Luo, C.Y. Yang, J.H. Gao, H.Y. Lin, Bio-orthogonal metabolic fluorine labeling enables deep-tissue visualization of tumor cells in vivo by F-19 magnetic resonance imaging, Anal. Chem. 94 (48) (2022) 16614–16621.

[9] A. Omidi, E. Weiss, M. Rosu, G. Thomas, J. Wilson, Quantification of radiotherapy-induced cardiac and aortic toxicity using magnetic resonance imaging in lung cancer, Int. J. Radiat. Oncol. 118 (1) (2024) E12.

[10] H. Hatabu, Y. Ohno, W.B. Gefter, G. Parraga, B. Madore, K.S. Lee, T.A. Altes, D. A. Lynch, J.R. Mayo, J.B. Seo, J.M. Wild, E.J.R. van Beek, M.L. Schiebler, H.-U. Kauczor, S. Fleischner, Expanding applications of pulmonary MRI in the clinical evaluation of lung disorders: Fleischner Society Position Paper, Radiology 297 (2) (2020) 286–301.

[11] Y.-H. Chi, J.-K. Hsiao, M.-H. Lin, C. Chang, C.-H. Lan, H.-C. Wu, Lung cancer-targeting peptides with multi-subtype indication for combinational drug delivery and molecular imaging, Theranostics 7 (6) (2017) 1612–1632.

[12] M. Doroudian, R. MacLoughlin, F. Poynton, A. Prina-Mello, S.C. Donnelly, Nanotechnology based therapeutics for lung disease, Thorax 74 (10) (2019) 965–976.

[13] X. Zhang, K. Jiang, S. Jiang, F. Zhao, P. Chen, P. Huang, J. Lin, In vivo near-infrared fluorescence/ratiometric photoacoustic duplex imaging of lung cancer-specific hNQO1, Anal. Chem. 94 (40) (2022) 13770–13776.

[14] A. Rong, H. Wang, C. Nie, Z. Han, M. Zhou, O.O. Atinuke, K. Wang, X. Wang, S. Liu, J. Zhao, W. Qiao, X. Sun, L. Wu, X. Sun, Glycerol-weighted chemical exchange saturation transfer nanoprobes allow ^{19}F/^{1}H dual-modality magnetic resonance imaging-guided cancer radiotherapy, Nat. Commun. 14 (1) (2023) 6644.

[15] C. Xu, S. He, X. Wei, J. Huang, M. Xu, K. Pu, Activatable sonoafterglow nanoprobes for T-cell imaging, Adv. Mater. 35 (30) (2023) 2211651.

[16] L. Liu, H.Y. Chu, J.K. Yang, P.Y. Ma, D.Q. Song, Construction of a magnetic-fluorescent-plasmonic nanosensor for the determination of MMP-2 activity based on SERS-fluorescence dual-mode signals, Biosens. Bioelectron. 212 (2022) 1143899.

[17] Y. Geng, H. Zhang, G. Zhang, J. Zhou, M. Zhu, L. Ma, X. Wang, T.D.D. James, Z. Wang, Near-infrared fluorescent probe for the in situ visualization of oxidative stress in the brains of neuroinflammatory and schizophrenic mice, Anal. Chem. 95 (32) (2023) 11943–11952.

[18] B. Li, S. Yu, R. Feng, Z. Qian, K. He, G.-J. Mao, Y. Cao, K. Tang, N. Gan, Y.-X. Wu, Dual-mode gold nanocluster-based nanoprobe platform for two-photon fluorescence imaging and fluorescence lifetime imaging of intracellular endogenous miRNA, Anal. Chem. 95 (40) (2023) 14925–14933.

[19] Y. Wang, Y.S. Wu, K. Li, S.H. Shen, Z.Y. Liu, D.C. Wu, Ultralong circulating lollipop-like nanoparticles assembled with gossypol, doxorubicin, and polydopamine via π-π stacking for synergistic tumor therapy, Adv. Funct. Mater. 29 (1) (2019) 1805582.

[20] W. Li, L. Sun, X. Zheng, F. Li, W. Zhang, T. Li, Y. Guo, D. Tang, Multifunctional nanoprobe based on fluorescence resonance energy transfer for furin detection and drug delivery, Anal. Chem. 95 (2023) 9654–9662.

[21] X. Su, C. Chan, J. Shi, M.-K. Tsang, Y. Pan, C. Cheng, O. Gerile, M. Yang, A graphene quantum Dot@Fe$_3$O$_4$@SiO$_2$ based nanoprobe for drug delivery sensing and dual-modal fluorescence and MRI imaging in cancer cells, Biosens. Bioelectron. 92 (2017) 489–495.

[22] W. Long, S. Li, Y. Yang, A. Chen, M. Xu, H. Zhai, T. Cai, Y. Peng, Self-cross-linked chitosan/albumin-bound nanoparticle hydrogel for inhibition of postsurgery malignant glioma recurrence, ACS Appl. Mater. Inter. 15 (49) (2023) 56774–56785.

[23] N.M. de Vasconcelos, N. Van Opdenbosch, H. Van Gorp, R. Martin-Perez, A. Zecchin, P. Vandenabeele, M. Lamkanfi, An apoptotic caspase network safeguards cell death induction in pyroptotic macrophages, Cell Rep. 32 (4) (2020).

[24] M. Poreba, A. Szalek, P. Kasperkiewicz, W. Rut, G.S. Salvesen, M. Drag, Small molecule active site directed tools for studying human caspases, Chem. Rev. 115 (22) (2015) 12546–12629.

[25] L. Jiang, H.-Y. Chen, C.-H. He, H.-B. Xu, Z.-R. Zhou, M.-S. Wu, E.K. Fodjo, Y. He, M. E. Hafez, R.-C. Qian, D.-W. Li, Dual-modal apoptosis assay enabling dynamic visualization of ATP and reactive oxygen species in living cells, Anal. Chem. 95 (2023) 3507–3515.

[26] L. Jiang, C.-H. He, H.-Y. Chen, C.-Y. Xi, E.K. Fodjo, Z.-R. Zhou, R.-C. Qian, D.-W. Li, M.E. Hafez, In situ monitoring of hydrogen peroxide released from living cells using a ZIF-8-based surface-enhanced raman scattering sensor, Anal. Chem. 93 (37) (2021) 12609–12616.

[27] Y. Huang, Y. Gu, X. Liu, T. Deng, S. Dai, J. Qu, G. Yang, L. Qu, Reusable ring-like Fe$_3$O$_4$/Au nanozymes with enhanced peroxidase-like activities for colorimetric-SERS dual-mode sensing of biomolecules in human blood, Biosens. Bioelectron. 209 (2022) 114253.

[28] Z. Tan, C. Zhu, L. Han, X. Liao, C. Wang, SERS and dark-field scattering dual-mode detection of intracellular hydrogen peroxide using biocompatible Au@COF nanosensor, Sensor. Actuat. B-Chem 373 (2022) 132770.

[29] X. Qin, J. Zhang, B. Wang, G. Xu, X. Yang, Z. Zou, C. Yu, Ferritinophagy is involved in the zinc oxide nanoparticles-induced ferroptosis of vascular endothelial cells, Autophagy 17 (12) (2021) 4266–4285.

[30] X. Sun, Y. Zhang, J. Li, K.S. Park, K. Han, X. Zhou, Y. Xu, J. Nam, J. Xu, X. Shi, L. Wei, Y.L. Lei, J.J. Moon, Amplifying STING activation by cyclic dinucleotide-manganese particles for local and systemic cancer metalloimmunotherapy, Nat. Nanotechnol. 16 (11) (2021) 1260–1270.

[31] M. Zhang, R. Song, Y. Liu, Z. Yi, X. Meng, J. Zhang, Z. Tang, Z. Yao, Y. Liu, X. Liu, W. Bu, Calcium-overload-mediated tumor therapy by calcium peroxide nanoparticles, Chem 5 (8) (2019) 2171–2182.

[32] P. Zheng, B. Ding, R. Shi, Z. Jiang, W. Xu, G. Li, J. Ding, X. Chen, A multichannel Ca^{2+} nanomodulator for multilevel mitochondrial destruction-mediated cancer therapy, Adv. Mater. 33 (15) (2021) 2007426.

[33] M. Wang, B. Zhou, L. Wang, F. Zhou, N. Smith, D. Saunders, R.A. Towner, J. Song, J. Qu, W.R. Chen, Biodegradable pH-responsive amorphous calcium carbonate nanoparticles as immunoadjuvants for multimodal imaging and enhanced photoimmunotherapy, J. Mater. Chem. B 8 (36) (2020) 8261–8270.

[34] L. Liu, X.T. Li, H. Zhang, H.D. Chen, M.M.A. Abualrejal, D.Q. Song, Z.X. Wang, Six-in-one peptide functionalized upconversion@polydopamine nanoparticle-based ratiometric fluorescence sensing platform for real-time evaluating anticancer efficacy through monitoring caspase-3 activity, Sens. Actuat. B-Chem. 333 (2021) 129554.

[35] X.Y. Huang, Y.R. Liang, L.G. Ruan, J.C. Ren, Chemiluminescent detection of cell apoptosis enzyme by gold nanoparticle-based resonance energy transfer assay, Anal. Bioanal. Chem. 406 (23) (2014) 5677–5684.